

**Figure 13.** Field and modelled data for the hydrophone channel of OBS 32, for (a) the same five traces as shown in Fig. 7 and (b) the same trace as shown in Fig. 9. Predicted data are generated using the smooth starting model in Fig. 6(b) and the final FWI model shown in Fig. 10. The location of the peaks and troughs for the data predicted by the FWI model are closer to the observed data overall, and the relative amplitudes of the peaks and troughs are much better matched for traces 1–3 in panel (a).

velocity model, respectively. Data from longer offsets are included in this plot as data out to 15 km offset were input to inversions at this frequency. The match between predicted and observed phase is clearly significantly better for the final velocity model. In summary, the phase plots show no evidence of cycle-skipping and suggest that FWI is moving the velocity model towards a global not a local minimum.

Fig. 13(a) shows the same five traces as in Fig. 7. The observed traces are examples of data input to the inversion with the 750 ms window applied. The predicted data are generated from the starting and final FWI velocity models. The FWI model produces data that better match the observed: the travel times to individual peaks and troughs are closer overall, and there is significant improvement in the waveform match. For example, the amplitudes of the peaks and troughs in the later arrivals in traces 1–3 are all closer to the observed. Fig. 13(b) shows the same trace as in Fig. 9; here the traveltimes fit is much better for the FWI model and the amplitude match is about the same. Note that the starting model is the smoothed velocity model shown in Fig. 6(b), for which the predicted data is shown in Fig. 9(b).

Fig. 14 shows the change in misfit for each iteration for the final inversion strategy. The misfit is reduced by ~14 per cent for the first 10 iterations at 3 Hz and then, thereafter, reduces by ~5 per cent every 10 iterations. This relatively small reduction in misfit is in accordance with the observed improvement in match for individual traces (Fig. 13): the initial fit is quite good and the improvement is clear but often quite small.

While testing different inversion strategies for the field data, the same strategies (smoothing, window lengths, iteration sequence) were also applied to recover checkerboards of various sizes and depths within the velocity model. These checkerboard tests were run to verify that the adopted inversion strategy could recover the anomalies seen in the inverted velocity models. Fig. 15 shows depth slices (where depth is bsl) through checkerboards that were all recovered using the inversion strategy adopted in the final FWI models shown in Fig. 10. Fig. 15(a) shows the successful recovery of a  $1.5 \times 1.5 \times 1.0$ -km sized checkerboard that was placed between 2.8 and 3.8 km bsl. Below this depth only larger checkerboards could be recovered. Fig. 15(b) shows the recovery of a checkerboard that was 2.5-km wide and 2-km deep and placed between 3 and 5 km bsl; Figs 15(c)–(d) show the recovery of the same checkerboard located between 4.5 and 6.5 km bsl. The smaller checks are well recovered down to about 3.5 km bsl, and the larger checks are well recovered down to about 4.5 km bsl. Below this, the checks are partially recovered down to about 6 km bsl, by which we mean

that the velocity perturbations are at the correct location and have the correct sign, but the absolute size of the perturbation is not recovered. Hence, it can be concluded that, away from the model edges, the velocity structure in the final inversions is likely to be real, but the magnitude of the recovered anomalies is probably too small in deeper parts of the model.

To explore further whether the final inversions are robust and produce consistent results, two additional tests were performed. In the first, the final velocity model shown in Fig. 10 was used to generate synthetic data, which was then treated as the observed data and inverted using the original inversion strategy and starting model. Fig. 16 shows the results of this test above the original FWI model. Each of the depth slices have the same structural features and all the areas of high and low velocity are matched. The re-recovered velocity model is slightly smoother, and only about 80 per cent of the original velocity perturbation has been recovered. In this test, unlike for the field data, the observed data are noise free. Hence, the results shown in Fig. 16 suggest that the velocity anomalies obtained from inverting the field data are recoverable using the selected inversion strategy, and are not artefacts produced by noise within the field data. This test also suggests that our final inversion strategy will not fully recover the magnitude of the real velocity anomalies.

In the second test, a new starting model was generated by taking the velocity perturbations recovered by FWI, multiplying them by 1.5 and adding them to the original starting velocity model (Figs 17a–c). The inversion was performed again using the same input field data and with the original inversion strategy, but substituting this model as the starting model. Such an approach is useful in FWI since the inversion tends to head in the right direction but may take many iterations to get there. The process of multiplying the recovered perturbations by 1.5 can move the inversion more rapidly towards the global minimum. Figs 17(d)–(f) show that the inversion moves the recovered anomalies back towards the original FWI model (Figs 17g–i). The results of this test, together with the other quality assurance procedures that have been applied, lead us to the conclude that the velocity structure in our final velocity model is robust. The recovered features in the FWI model shown in Fig. 10 consistently appear in the inverted velocity models.

## DISCUSSION

The checkerboard tests shown in Fig. 15 indicate that FWI can improve the model resolution by 2–4 times over traveltime tomography. A suite of checkerboard tests were performed by Weekly *et al.* (2014), and these showed that traveltime tomography could recover  $2.5 \times 2.5 \times 1$ -km sized checks in the uppermost 2 km of the crust, and  $5 \times 5 \times 2$ -km checkerboards down to 3 km below the seafloor. The recovery of finer-scale structure in the FWI model shown in Figs 10(b), (d) and (f) is encouraging and suggests that the approach adopted here could be successfully applied to other relatively sparse data sets. The theoretical resolution for FWI is half the seismic wavelength (Pratt *et al.* 1996) which, for the final inversion frequency of 5.1 Hz, corresponds to ~300 m in the uppermost crust and ~750 m in the lower crust at the Endeavour ridge. The resolution of the FWI velocity models presented here, which correspond to about 1.5 km in the upper crust and 2.5 km in the lower crust (Fig. 15), indicate that we have only obtained about 1/3–1/5 of the potential resolution of this technology. A suite of additional inversions were attempted to improve the resolution, including many

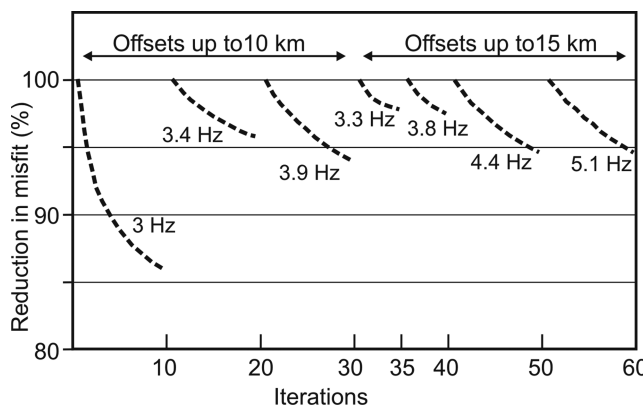
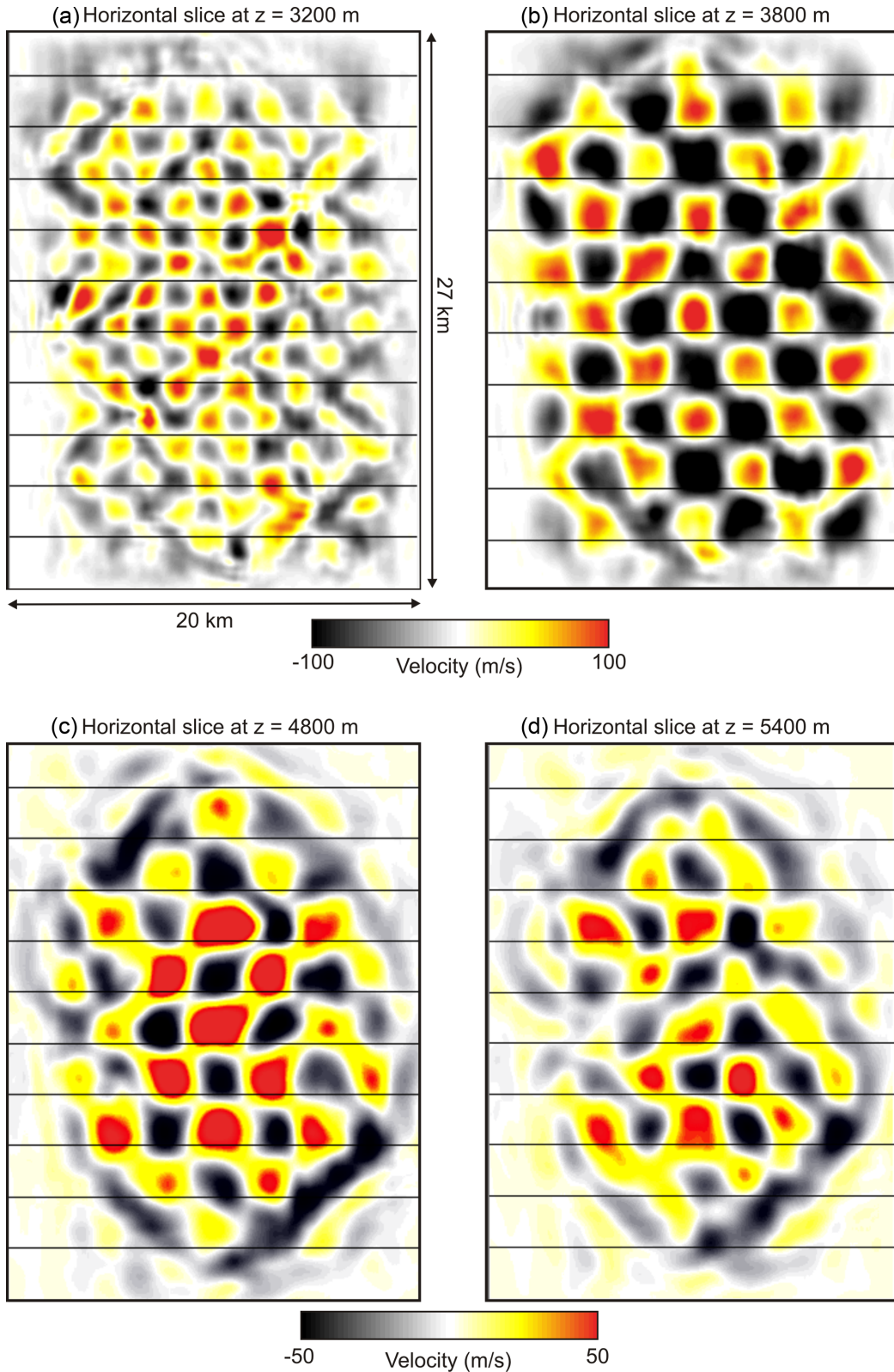
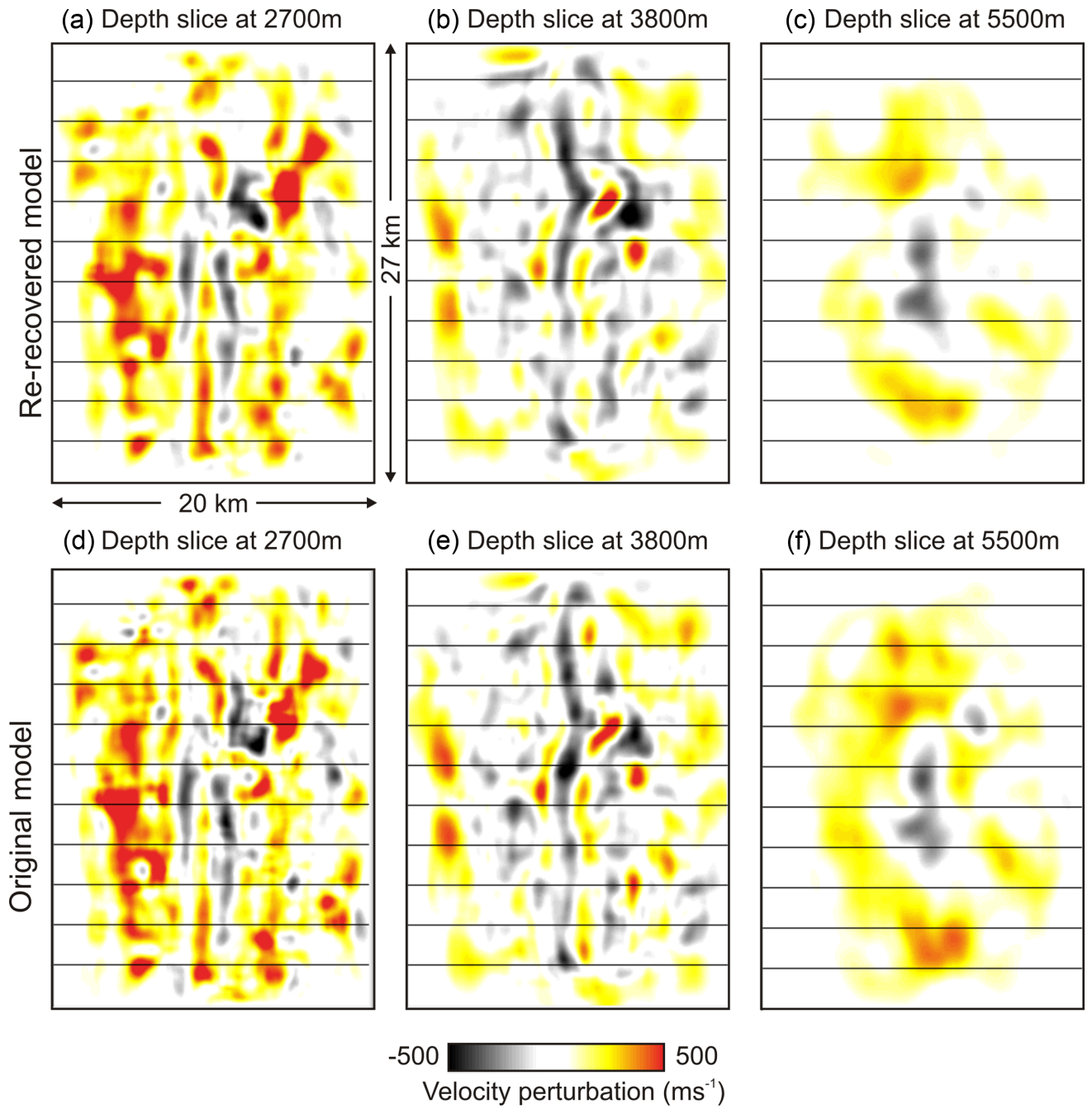


Figure 14. Plot showing the reduction in misfit at each iteration for the final inversion strategy used to recover the velocity model shown in Fig. 10.



**Figure 15.** Checkerboards at (a) 3200, (b) 3800, (c) 4800 and (d) 5400 m bsl, recovered using the same inversion strategy as in the final FWI model shown in Fig. 10. The checkerboard in panel (a) was 1.5 wide and 1.0 km deep and placed between 2.8 and 3.8 km bsl. In the other three plots, a checkerboard 2.5-km wide and 2-km deep was placed between (b) 3 and 5 km bsl and (c,d) 4.5 and 6.5 km bsl. The velocity perturbation was  $\pm 100 \text{ ms}^{-1}$ .



**Figure 16.** Depth slices showing velocity perturbation through: (a–c) a re-recovered and (d–f) original FWI velocity model at  $z = 2700, 3800$  and  $5500$  m bsl. In the re-recovered velocity model, the final velocity model shown in Fig. 10 was used to generate synthetic data, which were then treated as the observed data and inverted using the original inversion strategy and starting model. Each of the depth slices has the same structural features in the re-recovered and original FWI models, and all the areas of high and low velocity are matched.

more iterations and the inversion of higher frequencies, but the recovered finer-scale features were more variable and the available quality assurance procedures were unable to distinguish whether one of these models was definitely better than another. Resolution for the Endeavour data set is almost certainly affected by the data sparsity, and may also be limited by noise and the fact that the original starting model was unable to accurately predict the secondary arrivals.

In order to investigate how the full potential resolution of FWI could be obtained, a suite of checkerboard tests were performed to explore the effect of denser experimental geometries. Since the

expected resolution at 5 Hz is  $\sim 300$  m in the upper crust and  $\sim 750$  m in the lower crust, three checkerboards were placed in the model: a 300-m check was placed between 3000 and 3300 m, a 500-m check was placed between 4000 and 4500 m, and a 750-m check was placed between 5000 and 5750 m. Fig. 18 shows the recovered checkerboards for three experimental geometries: (a–c) OBS spacing of 1 km and shot spacing of 250 m, (d–f) OBS spacing of 2 km and shot spacing of 250 m, and (g–i) OBS spacing of 2.5 km and shot spacing of 400 m. Not surprisingly, the checkerboards are best recovered using the closest OBS and shot spacing, but the checkerboard is still partially recovered using the

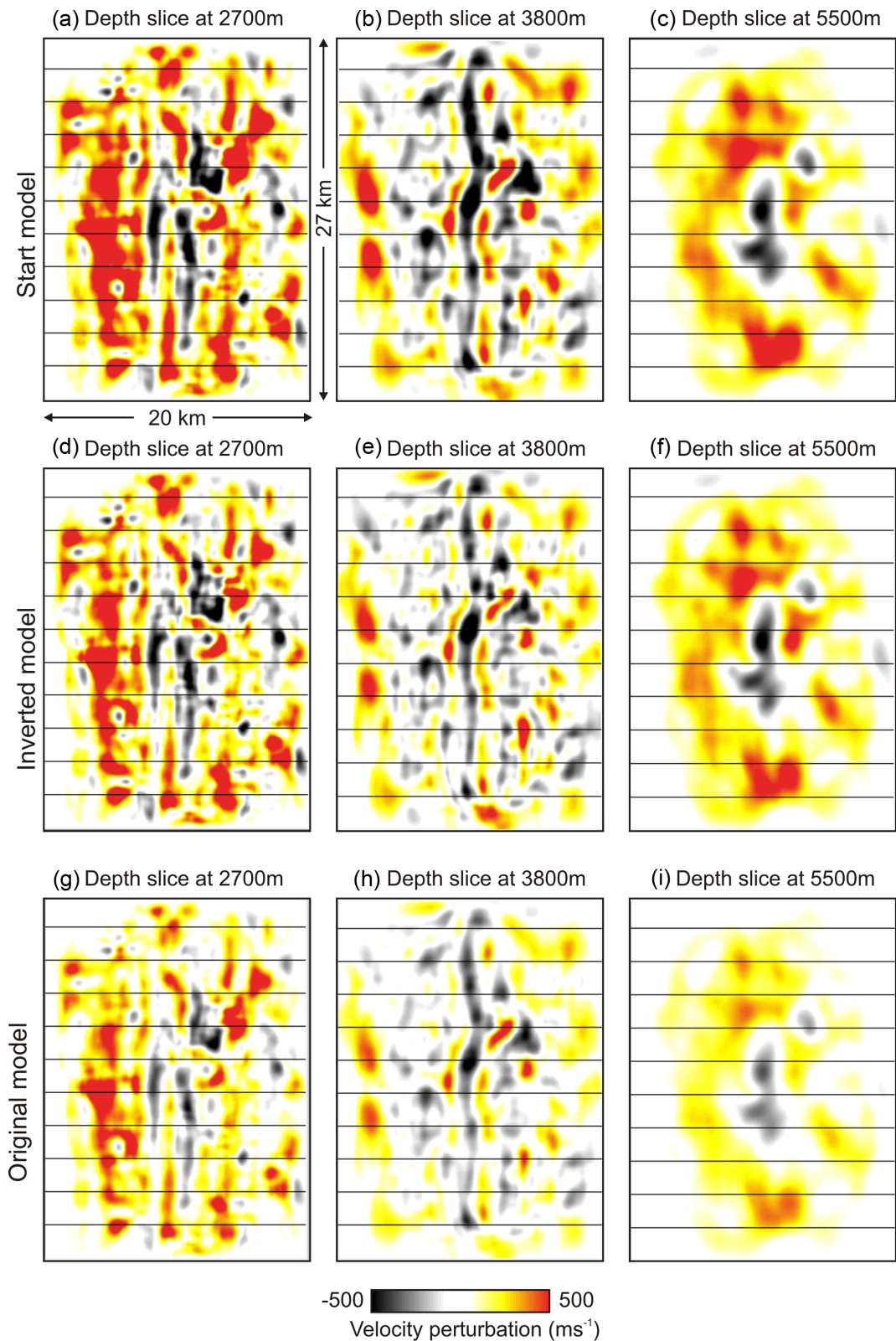


**Figure 17.** Horizontal slices at depths of 2700, 3800 and 5500 m bsl showing velocity perturbation relative to the original starting velocity model for (a–c) the FWI velocity model multiplied by 1.5; (d–f) FWI model obtained from inverting the field data using the perturbed velocity model shown in panel (a–c) as a starting model; and (g–i) the original FWI velocity model.

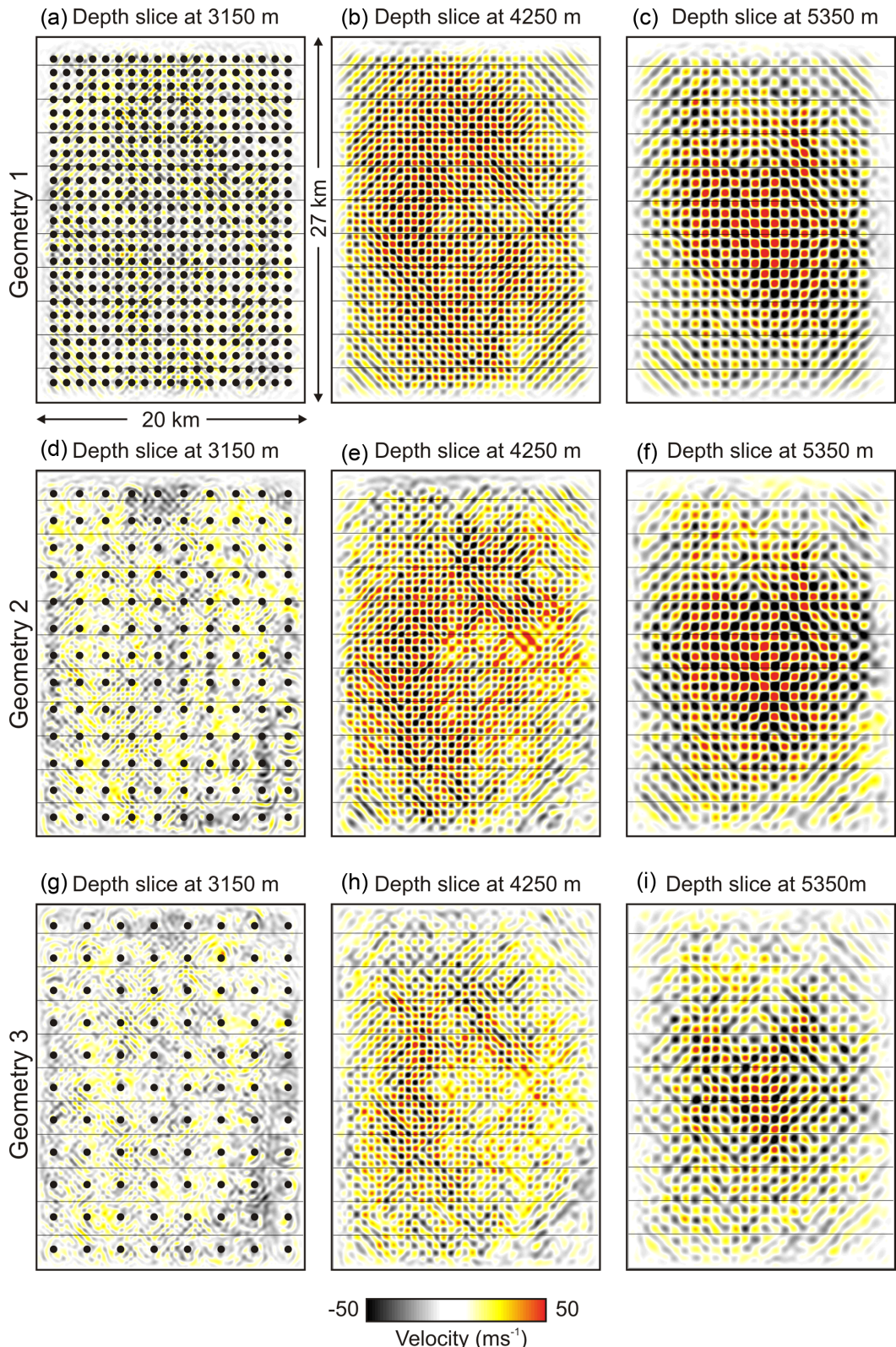


**Figure 18.** Recovered checkerboards for three experimental geometries: (a–c) OBS spacing of 1 km and shot spacing of 250 m, (d–f) OBS spacing of 2 km and shot spacing of 250 m, and (g–i) OBS spacing of 2.5 km and shot spacing of 400 m. OBS locations are shown as black dots; shots are located on a regular grid that extends a few hundred metres outside the OBS grid. There are three checkerboards in the model: (i) a 300-m check placed between 3000 and 3300 m bsl; (ii) a 500-m check placed between 4000 and 4500 m bsl; and (iii) a 750-m check placed between 5000 and 5750 bsl. The velocity perturbation was  $\pm 100 \text{ ms}^{-1}$ .

larger OBS and shot spacing. These tests suggest that we could obtain the full potential resolution of this technique using OBS spacings of between 2–2.5 km while inverting for frequencies up to 5 Hz.

## CONCLUSIONS

The inverted velocity anomalies in the final FWI model are roughly 2–4 times finer than can be recovered using traveltimes tomography. This improvement in resolution demonstrates that 3-D FWI can be used to recover fine-scale structure within the crust even when data are acquired using a relatively sparse shot and receiver spacing. In contrast to inversions performed on industrial data, additional regularization was required, with smoothing in both the horizontal and vertical directions. In addition, a laborious quality assurance procedure is needed to verify the validity of the adopted workflow, including checking the adequacy of the source wavelet and starting model, checking for problems with cycle skipping, investigating the effect of inputting different data bandwidths, window lengths and regularization, monitoring the progress of the inversion and performing additional model assessment. The full potential resolution of FWI could be obtained in future marine seismic surveys if data are collected using a 3-D acquisition geometry with a denser OBS spacing than is typical for academic surveys.

## ACKNOWLEDGEMENTS

Two reviewers made constructive comments that helped improve the manuscript. Imperial College London wishes to thank the sponsors of the FULLWAVE consortia: BG, BP, Chevron, CGGVeritas, ConocoPhillips, DONG, DownUnder GeoSolutions, ENI, HESS, Maersk, Nexen, PGS, Rio Tinto, Statoil, Sub Salt Solutions, TGS, Tullow Oil and Woodside for support in developing the 3-D FWI software. The 3-D ProMAX/SeisSpace package, supplied by Halliburton Software and Services, a Halliburton Company, under a university software grant, was used to pre-process and analyse the field and synthetic data. The inversion software used in this study is available for application to academic problems through collaboration with Imperial College London, and to commercial partners through membership of the FULLWAVE consortium. The experiment and analysis were supported by the National Science Foundation (NSF) under grants numbered OCE-0454700 to the University of Washington and OCE-0454747 and OCE-0651123 to the University of Oregon. The Department of Geological Sciences, University of Oregon, supported the academic visits by Arnoux and VanderBeek to Imperial College London. The data used in this research were provided by instruments from the Ocean Bottom Seismograph Instrument Pool (<http://www.obsip.org>) which is funded by the NSF. OBSIP data are archived at the IRIS Data Management Center (<http://www.iris.edu>).

## REFERENCES

- Arnoux, G., VanderBeek, B., Morgan, J., Hooft, E., Toomey, D., Wilcock, W. & Warner, M., 2014. Advanced seismic studies of the endeavour ridge: understanding the interplay among magmatic, hydrothermal, and tectonic processes at mid-ocean ridges, *AGU Fall Meeting*, abstr. # V31B-4751.
- Arnoux, G., VanderBeek, B., Morgan, J., Toomey, D., Hooft, E., Wilcock, W. & Warner, M., 2016. Seismic constraints on the magmatic-hydrothermal reaction zone beneath a mid-ocean ridge, *Nature Communications*, in press.
- Bansal, R. et al., 2013. Full wavefield inversion of ocean bottom node data, in *75th EAGE Conference, Extended Abstracts*, doi:10.3997/2214-4609.20130828.
- Bohnenstiehl, D.R., Dziak, R.P., Tolstoy, M., Fox, C.G. & Fowler, M., 2004. Temporal and spatial history of the 1999–2000 Endeavour Segment seismic series, Juan de Fuca Ridge, *Geochem. Geophys. Geosyst.*, **5**(9), Q09003, doi:10.1029/2004GC000735.
- Brenders, A.J. & Pratt, R.G., 2007. Full waveform tomography for lithospheric imaging: results from a blind test in a realistic crustal model, *Geophys. J. Int.*, **168**, 133–151.
- Bunks, C., Saleck, F.M., Zaleski, S. & Chavent, G., 1995. Multiscale seismic waveform inversion, *Geophysics*, **60**, 1457–1473.
- Butterfield, D.A., McDuff, R.E., Mottl, M.J., Lilley, M.D., Lupton, J.E. & Massoth, G.J., 1994. Gradients in the composition of hydrothermal fluids from the Endeavour segment vent field: phase separation and brine loss, *J. geophys. Res.*, **99**, 9561–9583.
- Canales, J.P. et al., 2012. Network of off-axis melt bodies at the East Pacific Rise, *Nat. Geosci.*, **5**, 279–283.
- Carbotte, S.M., Nedimovic, M.R., Canales, J.P., Kent, G.M., Harding, A.J. & Marjanovic, M., 2008. Variable crustal structure along the Juan de Fuca Ridge: influence of on-axis hot spots and absolute plate motions, *Geochem. Geophys. Geosyst.*, **9**, Q08001, doi:10.1029/2007GC001922.
- Davis, E.E. & Lister, C.R.B., 1977. Heat flow measured over the Juan de Fuca Ridge: evidence for widespread hydrothermal circulation in a highly heat transportive crust, *J. geophys. Res.*, **82**, 4845–4860.
- Davis, E.E. & Villinger, H., 1992. Tectonic and thermal structure of the Middle Valley Sedimented Rift, Northern Juan de Fuca Ridge, in *Proc. Ocean Drill. Program, Initial Rep.*, Vol. 139, pp. 9–41, ed. Dearmont, L.H., Ocean Drill Program, College Station, TX.
- Delescluse, M., Nedimovic, M.L. & Louden, K.E., 2011. 2D waveform tomography applied to long-streamer MCS data from the Scotian Slope, *Geophysics*, **76**, B151–B163.
- DeMets, C., Gordon, R.G. & Argus, D.F., 2010. Geologically current plate motions, *Geophys. J. Int.*, **181**, 1–80.
- Dunn, R.A. & Toomey, D.R., 2001. Crack-induced seismic anisotropy in the oceanic crust across the East Pacific Rise (9°30'N), *Earth planet. Sci. Lett.*, **189**, 9–17.
- Durant, D.T. & Toomey, D.R., 2009. Evidence and implications of crustal magmatism on the flanks of the East Pacific Rise, *Earth planet. Sci. Lett.*, **287**, 130–136.
- Dunn, R.A., Lekic, V., Detrick, R.S. & Toomey, D.R., 2005. Three-dimensional seismic structure of the Mid-Atlantic Ridge (35°N): evidence for focused melt supply and lower crustal dike injection, *J. geophys. Res.*, **110**, B09101, doi:10.1029/2004JB003473.
- Guasch, L., Warner, M., Nangoo, T., Morgan, J., Umpleby, A., Stekl, I. & Shah, N., 2012. Elastic 3D full-waveform inversion, in *82nd Annual International Meeting, SEG, Expanded Abstracts*, doi:10.1190/segma2012-1239.1.
- Hooft, E.E.E. et al., 2010. A seismic swarm and regional hydrothermal and hydrologic perturbations: the northern Endeavour segment, February 2005, *Geochem. Geophys. Geosyst.*, **11**(12), Q12015, doi:10.1029/2010GC003264.
- Houbiers, M., Mispel, J., Knudsen, B.E. & Amundsen, L., 2013. FWI with OBC data from the Mariner field, UK – the impact on mapping sands at reservoir level, in *75th EAGE Conference, Extended Abstracts*, doi:10.3997/2214-4609.20130829.
- Johnson, H.P., Karsten, J.L., Delaney, J.R., Davis, E.E., Currie, R.G. & Chase, R.L., 1983. A detailed study of the Cobb Offset on the Juan de Fuca Ridge: evolution of the propagating rift, *J. geophys. Res.*, **88**, 2297–2315.
- Johnson, H.P., Hutnak, M., Dziak, R.P., Fox, C.G., Urcuyo, I., Cowen, J.P., Nabalek, J. & Fisher, C., 2000. Earthquake-induced changes in a hydrothermal system on the Juan de Fuca Ridge mid-ocean ridge, *Nature*, **407**, 174–177.
- Jones, C.E., Evans, M., Ratcliffe, A., Conroy, G., Jupp, R., Selvage, J.I. & Ramsey, L., 2013. Full waveform inversion in a complex geological setting - a narrow azimuth towed streamer case study from the Barents

- Sea, in *75th EAGE Conference*, Extended Abstracts, doi:10.3997/2214-4609.20130830.
- Kapoor, S., Vigh, D., Li, H. & Derharoutian, D., 2012. Full waveform inversion for detailed velocity model building, in *74th EAGE Conference*, Extended Abstracts, doi:10.3997/2214-4609.20148712.
- Kapoor, S., Vigh, D., Wiarda, E. & Alwon, S., 2013. Full waveform inversion around the world, in *75th EAGE Conference*, Extended Abstracts, doi:10.3997/2214-4609.20130827.
- Karsten, J.L. & Delaney, J.R., 1989. Hot spot-ridge crest convergence in the Northeast Pacific, *J. geophys. Res.*, **94**, 700–712.
- Kelley, D.S. et al., 2012. Endeavour Segment of the Juan de Fuca Ridge: one of the most remarkable places on Earth, *Oceanography*, **25**, 44–61.
- Li, H.Y., Vigh, D. & Kapoor, J., 2011. The contribution of wide azimuth point receiver acquisition to the success of full waveform inversion, in *81st Annual International Meeting*, SEG, Expanded Abstracts, pp. 2555–2559.
- Lilley, M.D., Butterfield, D.A., Lupton, J.E. & Olson, E.J., 2003. Magmatic events can produce rapid changes in hydrothermal vent chemistry, *Nature*, **422**, 878–881.
- Lu, R., Lazaratos, S., Wang, K., Cha, Y.H., Chikichhev, I. & Prosser, R., 2013. High-resolution elastic FWI for reservoir characterization, in *75th EAGE Conference*, Extended Abstracts, doi:10.3997/2214-4609.20130113.
- Morgan, J.V., Warner, M.R., Collins, G.S., Grieve, R.A.F., Christeson, G.L., Gulick, S.P.S. & Barton, P.J., 2011. Full waveform tomographic images of the peak ring at the Chicxulub impact crater, *J. geophys. Res.*, **116**, doi:10.1029/2010JB008015.
- Morgan, J., Warner, M., Bell, R., Ashley, J., Barnes, D., Little, R., Roelle, K. & Jones, C., 2013. Next-generation seismic experiments: wide-angle, multi-azimuth, three-dimensional, full-waveform inversion, *Geophys. J. Int.*, **195**, 1657–1678.
- Mothi, S., Schwarz, K. & Zhu, H., 2013. Impact of full-azimuth and long-offset acquisition on full waveform inversion in deep water Gulf of Mexico, in *75th EAGE Conference*, Extended Abstracts, doi:10.3997/2214-4609.20130826.
- Plessix, R.-E., 2008. Introduction: towards a full waveform inversion, *Geophys. Prospect.*, **56**, 761–763.
- Plessix, R.-E. & Perkins, C., 2010. Full waveform inversion of a deep water ocean bottom seismometer dataset, *First Break*, **28**(4), 71–78.
- Pratt, R.G., 1999. Seismic waveform inversion in the frequency domain, Part I: Theory and verification in a physical scale model, *Geophysics*, **64**, 888–901.
- Pratt, R.G. & Shipp, R.M., 1999. Seismic waveform inversion in the frequency domain, Part 2: Fault delineation in sediments using crosshole data, *Geophysics*, **64**, 901–913.
- Pratt, R.G., Song, Z.-M., Williamson, P. & Warner, M., 1996. Two-dimensional velocity models from wide-angle seismic data by wavefield inversion, *Geophys. J. Int.*, **124**, 323–340.
- Prieux, V., Brossier, R., Gholami, Y., Operto, S., Virieux, J., Barkved, O.I. & Kommedal, J.H., 2011. On the footprint of anisotropy on isotropic full waveform inversion: the Valhall case study, *Geophys. J. Int.*, **187**, 1495–1515.
- Prieux, V., Brossier, R., Operto, S. & Virieux, J., 2013. Multi-parameter full waveform inversion of multi-component ocean bottom cable data from the Valhall field. Part 1. Imaging compressional wave speed density and attenuation, *Geophys. J. Int.*, **194**, 1640–1664.
- Ratcliffe, A. et al., 2011. Full waveform inversion: a North Sea OBS case study, in *81st Annual International Meeting*, SEG, Expanded Abstracts, pp. 2384–2388.
- Selwood, C.S., Shah, H.M., Mika, J.E. & Baptiste, D., 2013. The evolution of imaging over Azeri, from TTI tomography to anisotropic FWI, in *75th EAGE Conference*, Extended Abstracts, doi:10.3997/2214-4609.20130831.
- Shah, N., Warner, M., Nangoo, T., Umpleby, A., Štekl, I., Morgan, J. & Guasch, L., 2012. Quality assured full-waveform inversion: ensuring starting model adequacy, in *82nd Annual International Meeting*, SEG, Expanded Abstracts, doi:10.1190/segeab.31.
- Shipp, R.M. & Singh, S.C., 2002. Two-dimensional full wavefield inversion of wide-aperture marine seismic streamer data, *Geophys. J. Int.*, **151**, 325–344.
- Shoberg, T., Stein, S. & Karsten, J., 1991. Constraints on rift propagation history at the Cobb Offset, Juan de Fuca Ridge, from numerical modeling of tectonic fabric, *Tectonophysics*, **197**, 295–308.
- Sirgue, L., 2006. The importance of low frequency and large offset in waveform inversion, in *68th Annual International Conference and Exhibition incorporating SPE EUROPEC*, EAGE, Extended Abstracts, doi:10.3997/2214-4609.201402146.
- Sirgue, L. & Pratt, R.G., 2004. Efficient waveform inversion and imaging: a strategy for selecting temporal frequencies, *Geophysics*, **69**, 231–248.
- Sirgue, L., Barkved, O.I., Dellinger, J., Etgen, J., Albertin, U. & Kommedal, J.H., 2010. Full waveform inversion: the next leap forward in imaging at Valhall, *First Break*, **28**(4), 65–70.
- Sirgue, L., Etgen, J. & Albertin, U., 2007. 3D full waveform inversion: wide versus narrow azimuth acquisitions, in *77th Annual International Meeting*, SEG, Expanded Abstracts, pp. 1760–1764.
- Tarantola, A., 1984. Inversion of seismic reflection data in the acoustic approximation, *Geophysics*, **49**, 1259–1266.
- Thomsen, L., 1986. Weak elastic anisotropy, *Geophysics*, **51**, 1954–1966.
- Toomey, D.R., Solomon, S.C. & Purdy, G.M., 1994. Tomographic imaging of the shallow crustal structure of the East Pacific Rise at 9°30'N, *J. geophys. Res.*, **99**, 24 135–24 157.
- Van Ark, E.M. et al., 2007. Seismic structure of the Endeavour Segment, Juan de Fuca Ridge: correlations with seismicity and hydrothermal activity, *J. geophys. Res.*, **112**, B02401, doi:10.1029/2005JB004210.
- Vigh, D., Jiao, K., Huang, M., Moldoveanu, N. & Kapoor, J., 2013a. Long-offset-aided Full-waveform Inversion, in *75th EAGE Conference*, Extended Abstracts, doi:10.3997/2214-4609.20130825.
- Virieux, J. & Operto, S., 2009. An overview of full-waveform inversion in exploration geophysics, *Geophysics*, **74**, WCC1–WCC26.
- Vigh, D., Jiao, K. & Watts, D., 2013b. Elastic full-waveform inversion using 4C data acquisition, in *75th EAGE Conference*, Extended Abstracts, doi:10.3997/2214-4609.20130114.
- Vigh, D., Kapoor, J. & Li, H., 2011. Full waveform inversion application in different geological settings, in *81st Annual International Meeting*, SEG, Expanded Abstracts, pp. 2374–2378.
- Warner, M.R., Morgan, J.V., Umpleby, A., Štekl, I. & Guasch, L., 2012. Which physics for full-wavefield inversion?, in *74th EAGE Conference and Exhibition incorporating EUROPEC 2012*, EAGE, Extended Abstracts, pp. 2994–2998.
- Warner, M.R. et al., 2013. Anisotropic 3D full-waveform inversion, *Geophysics*, **78**, doi:10.1190/GEO2012-0338.1.
- Weekly, R.T., Wilcock, W.S.D., Hooft, E.E.E., Toomey, D.R., McGill, P.R. & Stakes, D.S., 2013. Termination of a 6 year ridge-spreading event observed using a seafloor seismic network on the Endeavour Segment, Juan de Fuca Ridge, *Geochem. Geophys. Geosyst.*, **14**, 1375–1398.
- Weekly, R.T., Wilcock, W.S.D., Toomey, D.R., Hooft, E.E.E. & Kim, E., 2014. Upper crustal seismic structure of the Endeavour Segment, Juan de Fuca Ridge from travel time tomography: implications for oceanic crustal accretion, *Geochem. Geophys. Geosyst.*, **15**, 1296–1315.
- Wilcock, W.S.D., Hooft, E.E.E., Toomey, D.R., McGill, P.R., Barclay, A.H., Stakes, D.S. & Ramirez, T.M., 2009. The role of magma injection in localizing black smoker activity, *Nat. Geosci.*, **2**, 509–513.
- Yoon, K., Moghaddam, P., Blad, P.I., Warner, M. & Sheng, J., 2014. Full waveform inversion on jackdaw ocean bottom nodes data in North Sea, in *76th EAGE Conference*, Extended Abstracts, doi:10.3997/2214-4609.20141417.